

Visualizing coherent intermolecular dipole–dipole coupling in real space

Yang Zhang^{1*}, Yang Luo^{1*}, Yao Zhang^{1*}, Yun-Jie Yu¹, Yan-Min Kuang¹, Li Zhang¹, Qiu-Shi Meng¹, Yi Luo¹, Jin-Long Yang¹, Zhen-Chao Dong¹ & J. G. Hou¹

Many important energy-transfer and optical processes, in both biological and artificial systems, depend crucially on excitonic coupling that spans several chromophores^{1–9}. Such coupling can in principle be described in a straightforward manner by considering the coherent intermolecular dipole–dipole interactions involved^{10,11}. However, in practice, it is challenging to directly observe in real space the coherent dipole coupling and the related exciton delocalizations, owing to the diffraction limit in conventional optics. Here we demonstrate that the highly localized excitations that are produced by electrons tunnelling from the tip of a scanning tunnelling microscope, in conjunction with imaging of the resultant luminescence, can be used to map the spatial distribution of the excitonic coupling in well-defined arrangements of a few zinc-phthalocyanine molecules. The luminescence patterns obtained for excitons in a dimer, which are recorded for different energy states and found to resemble σ and π molecular orbitals, reveal the local optical response of the system and the dependence of the local optical response on the relative orientation and phase of the transition

dipoles of the individual molecules in the dimer. We generate an in-line arrangement up to four zinc-phthalocyanine molecules, with a larger total transition dipole, and show that this results in enhanced ‘single-molecule’ superradiance from the oligomer upon site-selective excitation. These findings demonstrate that our experimental approach provides detailed spatial information about coherent dipole–dipole coupling in molecular systems, which should enable a greater understanding and rational engineering of light-harvesting structures and quantum light sources.

Scanning tunnelling microscope (STM)-induced luminescence (STML; see Extended Data Fig. 1) enables nano-imaging beyond the diffraction limit, owing to the highly localized excitation by the tunnelling electrons. This makes it possible to obtain intensity-based photon-yield images^{12,13} (photon images) and energy-resolved spectroscopic images of a single molecule¹⁴. To extend these abilities to reveal fundamental properties of intermolecular interactions at the molecular level, we first realize molecule-specific exciton emission from single molecules. As illustrated in Fig. 1a, this realization involves using an

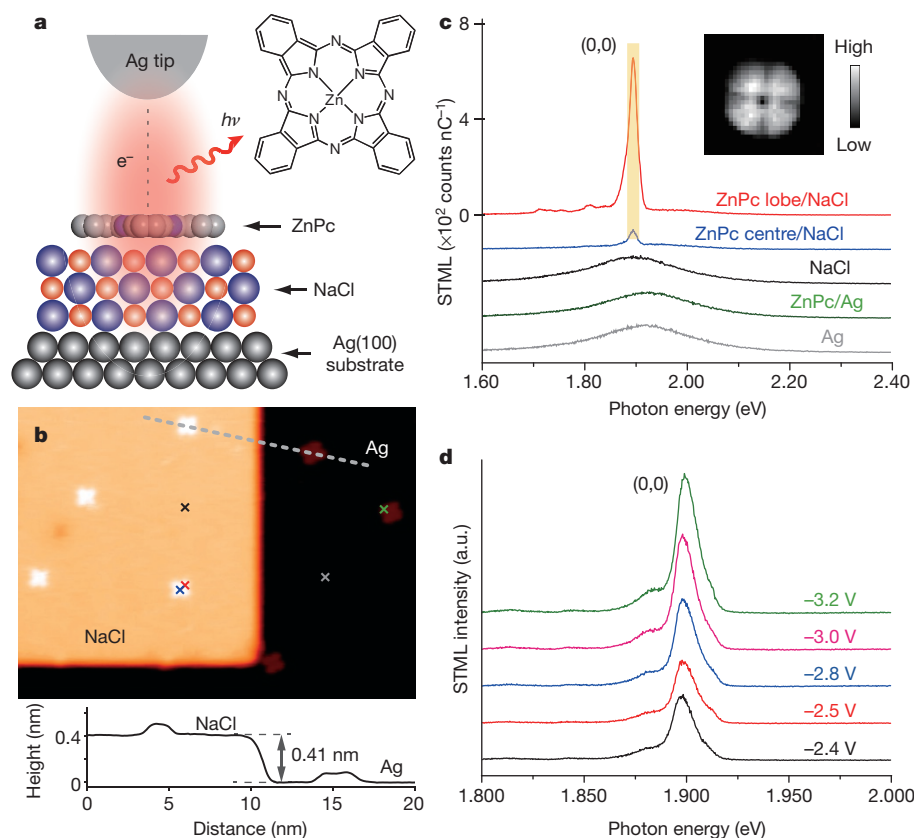


Figure 1 | Single-molecule electrochromism through electronic decoupling and nanocavity-plasmon enhancement. **a**, Schematic of STML from a ZnPc molecule on NaCl/Ag(100). Inset, ZnPc molecular structure. **b**, STM image showing isolated single ZnPc molecules adsorbed on either a three-monolayer NaCl island or bare Ag(100) (image size: 34 nm \times 25 nm; scanning parameters: -1.7 V, 2 pA). The height profile along the grey dashed line is given below the STM image. **c**, STML spectra acquired at the positions marked with an ‘x’ in **b** (-2.5 V, 200 pA, 60 s); the colour of the trace in **c** matches that of the corresponding ‘x’ in **b**. Inset, photon image of ZnPc on NaCl (-2.5 V, 200 pA, 5 s per pixel; 4 nm \times 4 nm, 30 \times 28 pixels; integrated over 1.89–1.91 eV, the yellow shaded energy region). For each pixel in the inset, a spectrum was recorded. The photon intensity integration is applied to each pixel (and each spectrum) for the selected energy range. **d**, STML spectra acquired above the molecular lobe on NaCl at different biases (200 pA, 60 s). a.u., arbitrary units. All STML spectra are offset for clarity; in **c**, the y-axis scale applies only to the red line. ‘(0,0)’ refers to the Q(0,0) transition.

¹Hefei National Laboratory for Physical Sciences at the Microscale and Synergetic Innovation Center of Quantum Information and Quantum Physics, University of Science and Technology of China, Hefei, Anhui 230026, China.

*These authors contributed equally to this work.

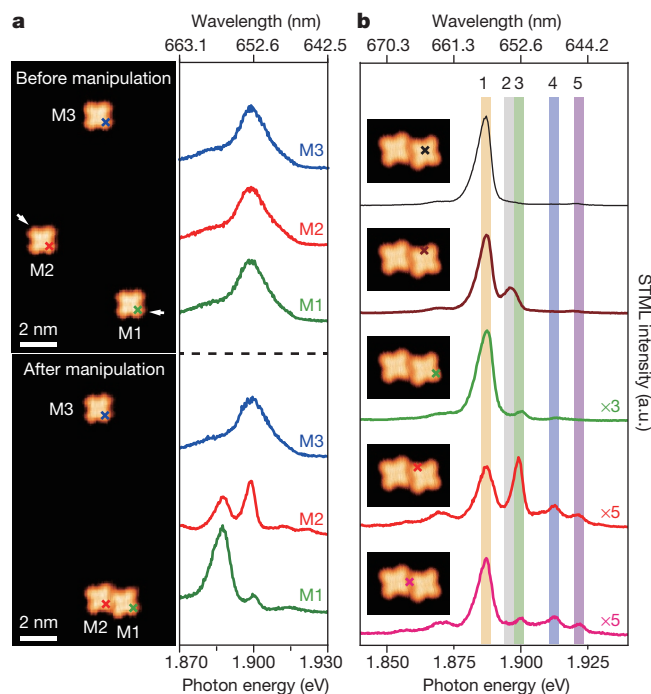


Figure 2 | Spectral evolution from isolated ZnPc monomers to an artificially constructed molecular dimer on NaCl. **a**, STM images (left; -1.7 V, 2 pA) and STML spectra (right; -2.5 V, 200 pA, 60 s) acquired before and after manipulation. Molecules M1 and M2 were pushed together, with the direction of motion indicated by the white arrows; molecule M3 was used as a reference. The STML spectra were acquired at the lobe positions marked with an 'x' in the STM images. **b**, Site-dependent STML spectra (-2.5 V, 200 pA, 60 s) acquired at the positions marked with an 'x' in the inset STM images (4 nm \times 3 nm; -1.7 V, 2 pA). All STML spectra are offset for clarity. The shaded bands labelled 1–5 indicate the peak positions and the ranges of integration used in Fig. 3b. a.u., arbitrary units.

ultrathin NaCl layer to electronically decouple zinc-phthalocyanine (ZnPc) molecules from the Ag(100) substrate to suppress substrate-induced fluorescence quenching^{15–21}; it also involves enhancing the spontaneous emission by resonant nanocavity plasmons (NCPs; red halo in Fig. 1a)^{22,23}. Images of isolated, single ZnPc molecules adsorbed on a three-monolayer NaCl island²⁴ and on bare Ag(100) both appear as four-lobe patterns (Fig. 1b), but excitation of adsorbed molecules through carrier injection (see Methods and Extended Data Fig. 2) generates detectable single-molecule fluorescence only in the case of decoupled ZnPc molecules (Fig. 1c). The sharp emission peak around 1.90 eV (approximately 653 nm) is assigned to the Q(0,0) transition of neutral ZnPc molecules on the basis of good agreement with the photoluminescence data of ZnPc in an argon matrix²⁵, the sharpness of the spectral feature that differs from the broadband emission of the NCP, and the nearly constant position of the peak when varying the excitation voltage (Fig. 1d)¹⁶.

Spectral measurements as a function of position (Fig. 1c) show that excitation over the ZnPc lobe generates emission with a much greater intensity than that generated from excitation above the ZnPc centre, probably owing to the dipole symmetry of the whole system¹⁴. This character is confirmed by the sub-nanometre-resolved spatial variations of optical transition probabilities in the photon image (Fig. 1c inset and Extended Data Fig. 3).

We next explore intermolecular excitonic coupling by pushing isolated ZnPc molecules together to create artificial molecular dimers (see Methods and Extended Data Fig. 4), which markedly changes the spectral features we observe (Fig. 2a). Differential conductance (dI/dV) spectra yield essentially the same electronic states for isolated monomers and the artificial dimer (Extended Data Fig. 5), so the spectral changes are not due to structural changes of the molecules. Moreover,

electronic coupling between two adjacent monomers in their ground state is very weak because the D_{4h} symmetry of the natural ZnPc molecule gives rise to a negligible permanent dipole.

A series of STML spectra collected at five different representative sites over the ZnPc dimer (Fig. 2b) shows that emission modes and intensities vary from site to site, and allows us to identify five major emission modes (marked in Fig. 2b) with narrower peak widths than those seen for the isolated monomer. Peak 1 (approximately 657 nm) and peak 2 (approximately 654 nm) are redshifted with respect to the monomer emission; almost no shift is observed for peak 3 (approximately 653 nm); peak 4 (approximately 648 nm) and peak 5 (approximately 645 nm) are blueshifted. (The origin of the additional emission peak at about 663 nm in Fig. 2b is discussed in Methods and Extended Data Fig. 6.)

For a more panoramic view of these five emission modes (indicated by arrows in Fig. 3a), we carried out spatially resolved spectroscopic imaging over the constructed dimer and obtained photon imaging patterns with noticeably different features for the different emission modes (Fig. 3b). The five photon imaging patterns, each with distinct numbers and positions of emission maxima and nodes, all differ from the photon imaging pattern of the isolated monomer. This, along with the occurrence of both blue- and redshifting of emission modes, suggests coherent excitonic coupling as the cause of the spectral changes observed upon dimer formation.

For a coherently coupled dimer with one of the monomers excited, two new one-exciton eigenstates formed via resonance interaction can be expressed as¹⁰

$$\Psi_{\text{dim},e} = (\psi_{1,e}\psi_{2,g} \pm \psi_{1,g}\psi_{2,e})/\sqrt{2} \quad (1)$$

in which Ψ and ψ represent the wavefunctions of the dimer and the monomer unit, respectively; the subscripts 'e' and 'g' denote the excited and ground states. The optical transition energy for the dimer (ΔE_{dim}) is (see Fig. 3c)

$$\Delta E_{\text{dim}} = \Delta E_{\text{mono}} + \Delta W \pm |J| \quad (2)$$

in which ΔE_{mono} represents the optical transition energy for an isolated monomer, ΔW represents the energy difference of van der Waals interaction between the excited and ground states of the dimer, and $|J|$ represents the exciton coupling strength. Within the point-dipole approximation^{10,26}, J can be expressed as

$$J = \frac{\boldsymbol{\mu}_1 \cdot \boldsymbol{\mu}_2}{4\pi\epsilon_0 r^3} - \frac{3(\boldsymbol{\mu}_1 \cdot \mathbf{r})(\boldsymbol{\mu}_2 \cdot \mathbf{r})}{4\pi\epsilon_0 r^5} \quad (3)$$

in which $\boldsymbol{\mu}_{1,2}$ are the transition dipoles of the component monomers (with amplitude μ_0), \mathbf{r} is the position vector between the two monomer centres ($|\mathbf{r}| = r$ is its magnitude) and ϵ_0 is the vacuum permittivity.

Each ZnPc molecule possesses two degenerate excited states and, hence, two associated equivalent transition-dipole orientations (x and y), owing to D_{4h} symmetry (Fig. 3d). Consequently, there are five possible dipole coupling modes for a molecular dimer: in-line in-phase ($\rightarrow\rightarrow$), in-line out-of-phase ($\rightarrow\leftarrow$), parallel in-phase ($\uparrow\uparrow$), parallel out-of-phase ($\uparrow\downarrow$) and orthogonal ($\uparrow\rightarrow$ and $\rightarrow\uparrow$). According to equation (3), the corresponding J for different dipole phase relations is

$$J_{\rightarrow\rightarrow} = -\frac{2\mu_0^2}{4\pi r^3} = -J_{\leftarrow\leftarrow}, J_{\uparrow\uparrow} = \frac{\mu_0^2}{4\pi r^3} = -J_{\downarrow\downarrow}, J_{\uparrow\rightarrow} = J_{\rightarrow\uparrow} = 0 \quad (4)$$

On the basis of the sequence of the energy levels and the coupling strength predicted by equations (2) and (4) for different modes, the emission peaks in Fig. 3a are assigned according to the exciton splitting diagram in Fig. 3d. The coupling strength ($|J|$) and the energy shift (ΔW) for different coherent dipole–dipole coupling modes can be directly measured (see Methods and Extended Data Table 1).

Insight into the coherent dipole–dipole coupling behaviour is thus obtained through the combined use of sub-nanometre-resolved

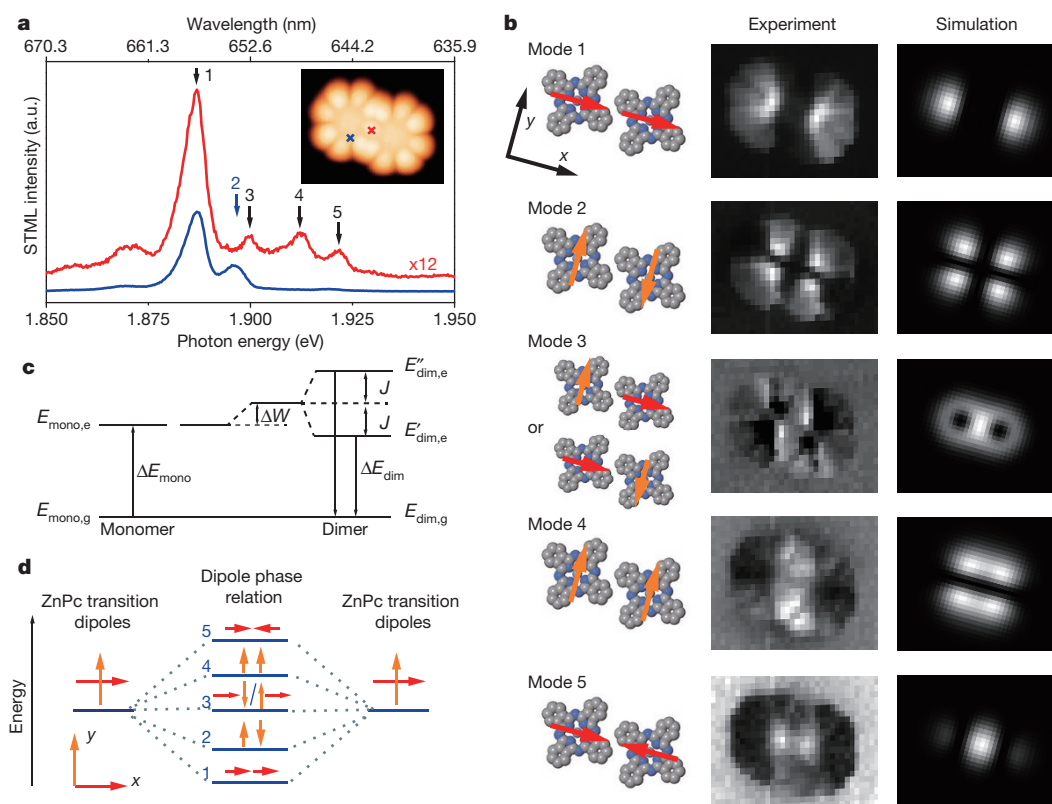


Figure 3 | Real-space visualization of coherent intermolecular dipole-dipole coupling in a constructed ZnPc dimer. **a**, STML spectra (-2.5 V, 200 pA, 60 s) acquired at the positions marked with an 'x' in the inset STM image (5 nm \times 4 nm; -2.5 V, 2 pA), showing five distinct emission modes (as indicated); the colour of the trace matches that of the corresponding 'x' in the inset. a.u., arbitrary units. **b**, Left, schematic arrangements of the transition dipoles. The red and orange arrows represent the in-line dipole along the dimer axial direction and the parallel dipole perpendicular to the dimer axial direction, respectively, which are superimposed on the molecular units. Middle, energy-resolved photon images for the five modes indicated in **a** (-2.5 V, 200 pA, 5 s per pixel; 5 nm \times 4 nm, 34×22 pixels; integration ranges for modes 1–5: $1,887 \pm 1.5$ meV, $1,896 \pm 1.5$ meV, $1,899 \pm 1.5$ meV, $1,912 \pm 1.5$ meV and $1,922 \pm 1.5$ meV, respectively, as indicated by the correspondingly labelled, shaded regions in Fig. 2b).

Right, corresponding simulated patterns. **c**, Exciton band energy diagram of a molecular dimer. $E_{\text{mono,e/g}}$, excited-/ground-state energy of an isolated monomer; ΔE_{mono} , optical transition energy for an isolated monomer; $E_{\text{dim,g}}$, ground-state energy of the dimer; $E'_{\text{dim,e}}$ and $E''_{\text{dim,e}}$, low-lying and high-lying excited-state energy of the dimer for similar coupling modes with opposite phases; ΔE_{dim} , optical transition energy for the dimer; ΔW , energy difference of van der Waals interaction between the excited and ground states of the dimer; J , exciton coupling strength. The horizontal line between that for $E_{\text{mono,e}}$ and ΔW refers to a hypothetical energy level of the dimer without any interactions; the horizontal line above ΔW refers to a hypothetical energy level without dipole coupling; the dashed lines serve as guides for the eye indicating the energy difference specified. **d**, Exciton splitting diagram for different coherent dipole-dipole coupling modes; the numbers correspond to the modes in **a** and **b**.

real-space visualization of local optical responses for different modes and theoretical simulations in Fig. 3b. The simulated photon imaging patterns show spatially resolved optical transition probabilities for various coupling modes based on the consideration of emission processes alone (see Methods and Extended Data Fig. 7). These simulated patterns capture the number and position of the emission maxima and nodes in the different experimentally observed patterns when considering that the transition-dipole orientations of the two monomers become parallel or perpendicular to the centre-to-centre axial direction upon dimer formation. This result indicates that the photon image for each mode is determined mainly by the emission process and its dependence on the molecular transition-dipole arrangements and their couplings, and that only minor features in the images arise as a result of changes in the spatial distribution of the local electronic density of states caused by modification of local excitation efficiencies (see Methods).

The in-line (parallel) dipole coupling patterns, which resemble σ -type (π -type) orbital bonding/anti-bonding patterns in molecular orbital theory (Extended Data Fig. 8), reflect directly, and in real space, the coherent nature of the dipole-dipole coupling for the different modes. These mode-specific patterns also serve as 'fingerprints' to aid spectral assignments, by identifying the physical origin of complicated optical transitions in molecular systems (see Methods and Extended Data Fig. 6).

The transition dipole arrangements in the dimer (as sketched in Fig. 3b) classify mode 1 and mode 4 as superradiant modes, owing to in-phase dipole coupling. In particular, the emission intensity for mode 1 at its brightest spots is much stronger than emission from any other modes, probably owing to an in-line and in-phase dipole coupling that results in the largest total dipole and the expected largest population probability at the lowest energy level. Surprisingly, we detect photon emission from mode 2 and mode 5 even though they show out-of-phase dipole coupling and are thus expected to be dark, subradiant modes; the observation of these subradiant modes is probably the result of the asymmetric image-dipole effect caused by the near-field tip generating a dipole component along the tip axial direction. It is the simultaneous observation of super- and subradiant emission modes that allows us to directly measure the dipole coupling strength $|J|$ (see Methods).

The initial excitation in STML occurs directly underneath the STM tip—in this case, in only one of the monomers, owing to the highly localized nature of the tunnelling electrons and the excitations they induce. The coherence evident in both the spectrally and spatially resolved data described above indicates that the excitation energy is rapidly shared between the two coupled monomers, and oscillated back and forth to yield an entangled dimer. The oscillation frequency Ω (ref. 27; see Methods and Extended Data Table 1),

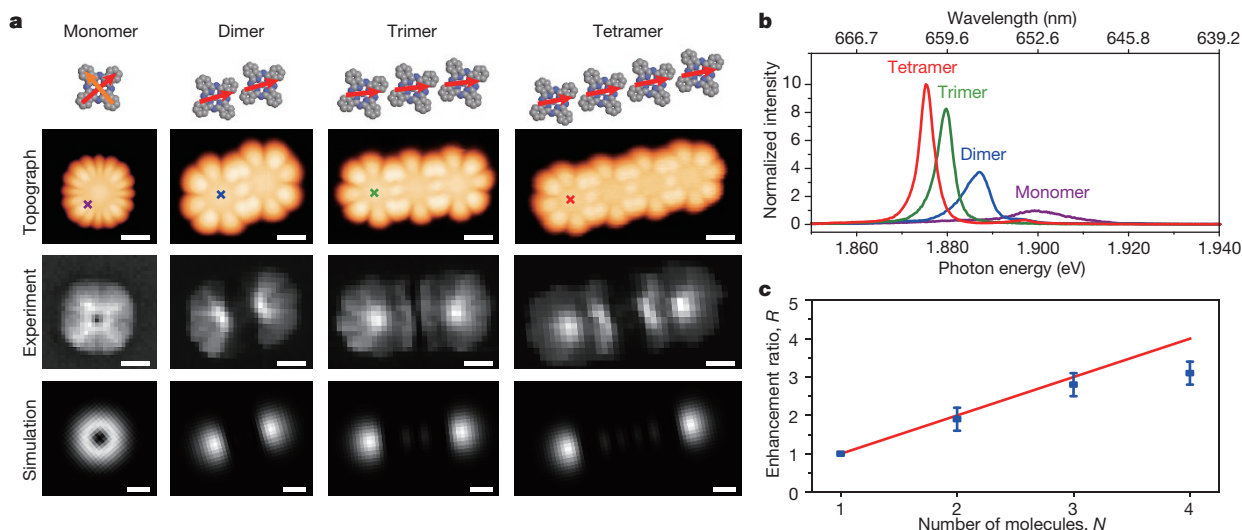


Figure 4 | Engineering electrically driven ‘single-molecule’ superradiance. **a**, First row, schematic arrangements of molecular structures and transition dipoles. Second row, STM images (-2.5 V, 2 pA). Third row, experimental photon images of the superradiant modes of the oligomers (-2.5 V, 200 pA, 5 s per pixel; pixel resolution (left to right): 30×28 , 34×24 , 34×21 and 40×18 ; integration ranges (left to right): $1,899 \pm 1.5$ meV, $1,887 \pm 1.5$ meV, $1,880 \pm 1.5$ meV and $1,875 \pm 1.5$ meV). Fourth row, simulated patterns based on in-line in-phase coupled dipole models. Scale bars, 1 nm. **b**, Typical STML spectra acquired at the positions marked by an ‘ \times ’ in the second row of **a** (-2.5 V,

200 pA, 60 s), normalized by the peak maximum of neighbouring, isolated ZnPc monomers to exclude the tip-induced intensity fluctuations. **c**, The emission enhancement ratio R for the superradiant mode of oligomers as a function of the number of molecules N (blue squares). The red line represents the ideal $R = N$ relation. R is calculated by dividing the integrated intensity of the oligomer emission over 1.86 – 1.94 eV by that of the monomer emission for ten data sets, and taking the average, yielding $R = 1$, $1.9(3)$, $2.8(3)$ and $3.1(3)$ for the monomer, dimer, trimer and tetramer, respectively, with the numbers in parentheses and error bars indicating the standard deviation.

deduced from the measured $|J|$, is of the order of 10^{13} s^{-1} , which is faster than the vibrational relaxation of the molecules (about 10^{12} s^{-1} ; ref. 28), and thus enables exciton delocalization and the generation of coherent signals²⁹. In this context, efficient decoupling of the emitter from the metallic substrate through the thin NaCl spacer layer is crucial for facilitating the observation of the coherent dipole–dipole coupling.

Guided by the knowledge gained from studying the dimer, and inspired by the prospect that superradiant modes might enable us to engineer bright, ‘single-molecule’ photon sources, we also explore the optical properties of larger entangled systems. Because in-line in-phase dipole coupling (that is, mode 1) should result in a large total dipole and yield strong superradiance, we arrange several molecules in a line to create oligomer architectures containing up to four molecules. This is illustrated in Fig. 4a, which also shows experimental and simulated photon imaging patterns for an isolated monomer and for the in-line in-phase superradiant mode of the dimer, trimer and tetramer. The STML spectra acquired in each system at the brightest spot (that marked with an ‘ \times ’ in Fig. 4a) are compared in Fig. 4b, which shows that the emission intensities increase as the number of component monomers increases. This finding is expected for an increase in total dipole moment, which is theoretically predicted when increasing the number of monomers. The σ -type anti-bonding-like patterns seen in the photon images of the trimer and tetramer, together with the further redshifted peaks due to stronger excitonic coupling, suggest that coherence is well maintained in these multi-molecule systems. The emission enhancement ratio (R) is expected to equal the number of monomers (N) in the coupled oligomer³⁰, but we find that our data deviate from this linear relation for the largest oligomer studied (that is, $N > 3$). Although this effect, which might be due to the limited spatial extension of confined NCP fields under the tip and increased non-radiative decay, requires further study, the findings we report here clearly demonstrate that it is possible to visualize excitonic coupling in real space with sub-nanometre resolution. This capability will enable new opportunities for studying intermolecular interaction at the level of individual molecules.

Online Content Methods, along with any additional Extended Data display items and Source Data, are available in the online version of the paper; references unique to these sections appear only in the online paper.

Received 28 August 2015; accepted 11 February 2016.

- Scholes, G. D. & Rumbles, G. Excitons in nanoscale systems. *Nature Mater.* **5**, 683–696 (2006).
- Hettich, C. *et al.* Nanometer resolution and coherent optical dipole coupling of two individual molecules. *Science* **298**, 385–389 (2002).
- Würthner, F., Kaiser, T. E. & Saha-Möller, C. R. J-aggregates: from serendipitous discovery to supramolecular engineering of functional dye materials. *Angew. Chem. Int. Ed.* **50**, 3376–3410 (2011).
- Engel, G. S. *et al.* Evidence for wavelike energy transfer through quantum coherence in photosynthetic systems. *Nature* **446**, 782–786 (2007).
- Lippitz, M. *et al.* Coherent electronic coupling versus localization in individual molecular dimers. *Phys. Rev. Lett.* **92**, 103001 (2004).
- Unold, T., Mueller, K., Lienau, C., Elsaesser, T. & Wiek, A. D. Optical control of excitons in a pair of quantum dots coupled by the dipole-dipole interaction. *Phys. Rev. Lett.* **94**, 137404 (2005).
- Hildner, R., Brinks, D., Nieder, J. B., Cogdell, R. J. & van Hulst, N. F. Quantum coherent energy transfer over varying pathways in single light-harvesting complexes. *Science* **340**, 1448–1451 (2013).
- Diehl, F. P. *et al.* Emergence of coherence through variation of intermolecular distances in a series of molecular dimers. *J. Phys. Chem. Lett.* **5**, 262–269 (2014).
- Halpin, A. *et al.* Two-dimensional spectroscopy of a molecular dimer unveils the effects of vibronic coupling on exciton coherences. *Nature Chem.* **6**, 196–201 (2014).
- Kasha, M., Rawls, H. & Ashraf El-Bayoumi, M. The exciton model in molecular spectroscopy. *Pure Appl. Chem.* **11**, 371–392 (1965).
- Tretiak, S., Zhang, W. M., Chernyak, V. & Mukamel, S. Excitonic couplings and electronic coherence in bridged naphthalene dimers. *Proc. Natl Acad. Sci. USA* **96**, 13003–13008 (1999).
- Berndt, R. *et al.* Photon-emission at molecular resolution induced by a scanning tunneling microscope. *Science* **262**, 1425–1427 (1993).
- Chen, C., Bobisch, C. A. & Ho, W. Visualization of Fermi’s golden rule through imaging of light emission from atomic silver chains. *Science* **325**, 981–985 (2009).
- Chen, C., Chu, P., Bobisch, C. A., Mills, D. L. & Ho, W. Viewing the interior of a single molecule: vibronically resolved photon imaging at submolecular resolution. *Phys. Rev. Lett.* **105**, 217402 (2010).
- Qiu, X. H., Nazin, G. V. & Ho, W. Vibrationally resolved fluorescence excited with submolecular precision. *Science* **299**, 542–546 (2003).
- Dong, Z. C. *et al.* Vibrationally resolved fluorescence from organic molecules near metal surfaces in a scanning tunneling microscope. *Phys. Rev. Lett.* **92**, 086801 (2004).

17. Čavar, E. *et al.* Fluorescence and phosphorescence from individual C₆₀ molecules excited by local electron tunneling. *Phys. Rev. Lett.* **95**, 196102 (2005).
18. Kabakchiev, A., Kuhnke, K., Lutz, T. & Kern, K. Electroluminescence from individual pentacene nanocrystals. *ChemPhysChem* **11**, 3412–3416 (2010).
19. Lee, J., Perdue, S. M., Rodriguez Perez, A. & Apkarian, V. A. Vibronic motion with joint angstrom–femtosecond resolution observed through fano progressions recorded within one molecule. *ACS Nano* **8**, 54–63 (2014).
20. Reecht, G. *et al.* Electroluminescence of a polythiophene molecular wire suspended between a metallic surface and the tip of a scanning tunneling microscope. *Phys. Rev. Lett.* **112**, 047403 (2014).
21. Merino, P., Große, C., Roslowska, A., Kuhnke, K. & Kern, K. Exciton dynamics of C₆₀-based single-photon emitters explored by Hanbury Brown–Twiss scanning tunnelling microscopy. *Nature Commun.* **6**, 8461 (2015).
22. Dong, Z. C. *et al.* Generation of molecular hot electroluminescence by resonant nanocavity plasmons. *Nature Photon.* **4**, 50–54 (2010).
23. Rossel, F., Pivetta, M. & Schneider, W.-D. Luminescence experiments on supported molecules with the scanning tunneling microscope. *Surf. Sci. Rep.* **65**, 129–144 (2010).
24. Ploigt, H.-C., Brun, C., Pivetta, M., Patthey, F. & Schneider, W.-D. Local work function changes determined by field emission resonances: NaCl/Ag(100). *Phys. Rev. B* **76**, 195404 (2007).
25. Murray, C. *et al.* Visible luminescence spectroscopy of free-base and zinc phthalocyanines isolated in cryogenic matrices. *Phys. Chem. Chem. Phys.* **13**, 17543–17554 (2011).
26. Vlaming, S. M. & Eisfeld, A. Tunable superradiance in porphyrin chains on insulating surfaces. *J. Phys. D* **47**, 305301 (2014).
27. Lanzani, G. *The Photophysics behind Photovoltaics and Photonics* Ch. 3 (John Wiley & Sons, 2012).
28. Krishna, V. & Tully, J. C. Vibrational lifetimes of molecular adsorbates on metal surfaces. *J. Chem. Phys.* **125**, 054706 (2006).
29. Kasha, M. Energy transfer mechanisms and the molecular exciton model for molecular aggregates. *Radiat. Res.* **20**, 55–70 (1963).
30. Scully, M. O. & Svidzinsky, A. A. The super of superradiance. *Science* **325**, 1510–1511 (2009).

Acknowledgements We thank B. Wang for discussions. This work is supported by the National Basic Research Program of China, the Strategic Priority Research Program of the Chinese Academy of Sciences, the Natural Science Foundation of China, the Fundamental Research Funds for the Central Universities and Hefei Science Center of the Chinese Academy of Sciences.

Author Contributions Z.-C.D. and J.G.H. supervised the project. Yang Z., Yang L., Yao Z., Y.-J.Y., Y.-M.K., L.Z. and Q.-S.M. performed the experiments and analysed the data. Yang Z., Yang L., Yao Z., Yi L., J.-L.Y., Z.-C.D. and J.G.H. contributed to the interpretation of the data and theoretical simulations. Yang Z., Yi L., Z.-C.D. and J.G.H. co-wrote the manuscript. All authors discussed the results and commented on the manuscript.

Author Information Reprints and permissions information is available at www.nature.com/reprints. The authors declare no competing financial interests. Readers are welcome to comment on the online version of the paper. Correspondence and requests for materials should be addressed to Z.-C.D. (zcdong@ustc.edu.cn) or J.G.H. (jghou@ustc.edu.cn).

METHODS

Experimental section. Our experiments were performed with a custom low-temperature ultrahigh-vacuum STM (Unisoku) combined with optical detection systems at about 8 K under a base pressure of about 1×10^{-10} Torr. ZnPc molecules were thermally evaporated onto the Ag(100) substrate partially covered by NaCl islands²⁴ at about 8 K (Ag(100) was previously cleaned by argon ion sputtering and annealing). Electrochemically etched silver (Ag) tips used in all our experiments were cleaned by electron-bombarding and argon-ion sputtering, followed by further modification through voltage pulses to achieve the desired NCP modes. STM imaging and spectral measurements were taken in a constant-current mode with the sample biased. Spatially resolved spectroscopic imaging over molecular structures was carried out with each pixel recording a spectrum that provides energy-resolved optical transition probabilities^{31,32}. The photon collection and detection systems are detailed in Extended Data Fig. 1. dI/dV spectra and dI/dV mapping were measured using a lock-in technique.

Because STM is known to have versatile manipulation abilities^{33–35}, here the ZnPc molecular manipulation was realized via pushing by positioning the tip over the edge of a ZnPc lobe and decreasing the tip–molecule distance (for example, approaching 200 pm) at a positive bias of +2.5 V (Extended Data Fig. 4). The bias-dependent feature of the STM images from –1.7 V to –2.5 V is detailed in Extended Data Fig. 5.

Spatially and spectrally resolved photon images were obtained by recording a spectrum at each pixel and assigning to each pixel the integrated emission intensities over a certain wavelength range. The thermal drift issue should be considered for spectroscopic imaging experiments when the total acquisition time is long. The thermal drift of our current system at about 8 K is 0.1–0.2 nm h^{–1}. For the STM imaging with acquisition times of around 10–20 min, such drift can be neglected. However, for the spectroscopic imaging experiments, the total acquisition time could be as long as 1.5 h and the total drift value would be 0.15–0.3 nm, which is relatively large compared with the size of an individual ZnPc molecule. Therefore, to precisely correlate the emission feature with the molecular structure, we corrected the image distortion caused by the thermal drifts for all the photon imaging patterns given in the main text, as detailed in the following. When we acquired an energy-resolved spectroscopic image, a reference STM image for the same molecule was acquired simultaneously. The resultant, slightly deformed STM image was adjusted to match with the molecular features in an almost drift-free STM image for the same area that was acquired at a normal scanning speed (about 10 min per frame). The same adjustment parameters are applied to the corresponding photon imaging pattern.

Energy-level alignment and carrier-injection excitation. At –2.5 V (the voltage used for most of our experiments), the single-molecule electroluminescence is generated by the carrier-injection excitation in a double-barrier tunnelling junction. As shown in Extended Data Fig. 2, molecular electroluminescence increases as excitation bias increases from –1.8 V to –2.5 V in amplitude, in particular when the voltage approaches about –2.2 V, at which the highest occupied molecular orbital (HOMO) is aligned with the Fermi level of the tip (such that holes can be directly injected into the HOMO), as discussed below.

The energy-level alignments are deduced according to previously documented methods^{20,36,37}. The photon energy emitted from a single ZnPc is determined by the energy difference between the excited and ground states of the molecule, which is less than or equal to the HOMO–LUMO gap of the molecule (LUMO, lowest unoccupied molecular orbital). For the sake of simplicity, we assume that the HOMO–LUMO gap at zero bias ($V_b = 0$) is approximately equal to the optical gap associated with the (0,0) emission band at approximately 653 nm (about 1.9 eV), with the energy of the HOMO state represented by E_H and that of the LUMO state by E_L . By denoting the voltage drop repartition across the vacuum barrier as α , and referring to the onset voltages for the emergence of the HOMO and LUMO states in the dI/dV spectra, we have $E_L - E_H = 1.9$, $E_L = 0.6\alpha$ and $E_H = -2.2\alpha$. From these relations we deduce $\alpha = 0.68$, $E_H = -1.5$ eV and $E_L = 0.4$ eV with respect to the Fermi level ($E_0 = 0$) at $V_b = 0$ V. The energy-level alignments for $V_b = -2.2$ V and $V_b = +4.7$ V can also be deduced accordingly. That is why the emission intensity is evidently increased at about –2.2 V—the HOMO is now aligned with the Fermi level of the tip (and so holes can be directly injected into the HOMO). When a ZnPc molecule is excited at –2.5 V (the voltage used for most of our experiments), the excitation model based on the carrier injection is valid in terms of energy-level alignment. The LUMO and HOMO states fall inside the energy window between the Fermi levels of the tip and substrate. Thus, the electrons can be injected to the LUMO from the substrate while the electrons in the HOMO can tunnel out to the tip, generating holes in the HOMO. Then, the molecule-specific emission occurs through the recombination of the electron in the LUMO and the hole in the HOMO when the molecular excited state (exciton) decays back to the ground state.

When a ZnPc molecule is excited at positive bias such as +2.5 V, the molecular electroluminescence becomes very weak. The injection excitation mechanism would become a dominant process only for positive biases raised above +4.7 V,

at which both the LUMO and HOMO fall inside the energy window between the Fermi levels of the tip and substrate, as shown in Extended Data Fig. 2e. At such high voltages, the molecule can easily be moved or even damaged, making the measurements impossible.

Spectral evolution with varied intermolecular distances. In the experiments, the NaCl surface is not perfectly flat and the ZnPc is believed to move in a discontinuous manner by hopping between the surface lattice sites. The minimum displacement for manipulation is found to be about 0.4 nm, which is very close to the lattice constant of the NaCl surface³⁸. This makes it impossible to achieve continuous spectral evolution with varied intermolecular distances. We therefore acquired spectra at only a few representative intermolecular distances (r , centre-to-centre distance), as shown in Extended Data Fig. 4.

When $r \geq 4.0$ nm, no spectral changes in emission peaks are observed for the ZnPc lobes at the spectral-resolution limit of our current instruments (0.7 meV). When r was decreased to about 2.8 nm, some small spectral changes were observed (see STML spectrum on M2), which suggests the presence of some intermolecular coupling. When r was further decreased to about 2 nm, the emission peaks shifted or split and five emission modes were observed in STML spectra acquired at representative sites, as shown in Extended Data Fig. 4c. In this case, the measured emission-peak energies for modes 1 and 5 are approximately 1.893 eV and 1.912 eV, respectively, giving rise to a smaller exciton coupling strength $|J|$ of about 9.5 meV for the in-line coupling, as expected. However, it is hard to precisely deduce J for parallel coupling, because the mode-2, mode-3 and mode-4 emission peaks are heavily mixed together.

Assignment of the emission peak at about 1.870 eV for the ZnPc dimer. The emission peak at approximately 1.870 eV (about 663 nm) for the dimer (mode 1' in Extended Data Fig. 6b) originated from the in-line in-phase coupling of transition dipoles associated with the shoulder peak at approximately 1.882 eV (659 nm) for an isolated ZnPc monomer (Extended Data Fig. 6a). The latter peak is related to the vibronic structure of the Q band with relatively large Franck–Condon contribution^{39,40}. This assignment for the emission peak at approximately 1.870 eV for the ZnPc dimer is supported by two facts: (1) the photon imaging pattern of the peak (at approximately 1.870 eV) shown in Extended Data Fig. 6c is very similar to the σ -type anti-bonding-like feature of the imaging pattern for mode 1 in Fig. 3b; and (2) mode 1' is redshifted by about 17 meV with respect to mode 1, which is about the same as the redshift between the shoulder peak and the dominant Q(0,0) peak.

The emission intensity of mode 1' is much weaker than that of mode 1, although mode 1' is believed to be the strongest emission mode over all the modes that originate from the dipole–dipole coupling associated with the shoulder peak. If we assume that the ratio of the emission intensity between mode 2' (3', 4', 5') and mode 1' is the same as that between mode 2 (3, 4, 5) and mode 1, then the intensity of mode 2' (3', 4', 5') will be much weaker than that of mode 2 (3, 4, 5), making their emission features buried in the spectral background of modes 1–5.

Therefore, the dipole coupling associated with the shoulder peak at approximately 1.882 eV will not affect the spectral features from 1.88 eV to 1.93 eV for various modes of the dimer that are attributed to the contribution from the dominant Q-band emission peak (at about 1.899 eV).

The weak high-energy shoulder around 1.91 eV for the ZnPc monomer might be related to the rotation of ZnPc under the excitation. However, such a rotation is blocked for the dimer (as shown in Extended Data Fig. 5) and for oligomers, and so the high-energy shoulder in the monomer no longer exists.

The roles of excitation and emission processes on the photon images. The photon image is spectrally reconstructed from the photon-yield signal at each pixel, which is related to both the local excitation efficiency and the optical transition probability between two different electronic states. The excitation efficiency depends on the local electronic density of states under the carrier-injection excitation model, whereas the optical transition probability is decided by the emission process associated with molecular transition-dipole arrangements and their couplings.

In ref. 14, the important influence of the emission process on the pattern of photon images is demonstrated for a single molecule. More appealing evidence for the dominant role of the emission process in the photon image for each mode is found in our experiments for molecular dimers (or oligomers) involving more-than-one-transition dipoles and all their possible arrangements. As illustrated in Fig. 3b, different photon images are obtained for different emission modes, despite excitation under the same bias of –2.5 V (that is, the same distribution of local electronic density of states). Moreover, the mode-1 emission patterns of the trimer and tetramer in Fig. 4 are different to the corresponding dI/dV mappings shown in Extended Data Fig. 9.

The major feature of the photon image for each mode is similar to the theoretically simulated photon image in Fig. 3b that is based on emission processes alone (a similar theoretical treatment to that proposed in ref. 14), which further suggests that the major feature of the photon image for each mode is determined

by the emission process associated with molecular transition-dipole arrangements and their couplings.

Photon images acquired in constant-height and constant-current mode. The trajectory of the tip is known to affect the intra-molecularly resolved conductance images measured with a closed feedback loop (that is, constant-current mode) (see, for example, ref. 41). We examined the effect of such variation of tip-sample distance on the photon images. As shown in Extended Data Fig. 10, a special spectroscopic image with an open feedback loop (that is, constant-height mode) was collected. The resultant photon images for different modes were normalized by the tunnelling current pixel by pixel. The features of the normalized photon images acquired with an open feedback loop are almost the same as those acquired with a closed feedback loop. These results indicate that, in the spectroscopic imaging measurements with a closed feedback loop, the variations in tip-sample distance caused by the fluctuations of the molecular topography will not affect the major features of photon images.

Theoretical simulation of real-space STML mapping. For a single ZnPc molecule, the transition-dipole moment corresponding to the HOMO–LUMO transition, described by the transition density $\langle\psi_g|\psi_e\rangle$ (refs 42, 43) is calculated to be about 10.6 Debye (about 0.22 e-nm) using density functional theory (DFT)⁴⁴. To capture the physical essence and fit with the experimental patterns, we simplify the transition dipole of a single molecule to a pair of opposite point charges (each containing one electron charge) separated by 0.22 nm, as shown in Extended Data Fig. 7a. The centres of the charge pairs are placed in the centres of the ZnPc monomers. The distance between the centres of charge pairs in the dimer are chosen to be 1.45 nm, which is the centre-to-centre distance between two component ZnPc monomers measured in STM images.

The best agreement between experimental photon imaging patterns and simulated patterns is achieved when the transition-dipole orientations of ZnPc molecules in the dimer are chosen to be parallel or perpendicular to the dimer axial direction (centre-to-centre), as illustrated in Fig. 3 and Extended Data Fig. 7b. This orientation modification is probably associated with the symmetry breakdown from D_{4h} for the monomer to C_{2h} for the dimer.

A simple image-charge method was used to simulate real-space STML mapping. The introduction of a metallic plasmonic tip induces image charges on both the tip and the substrate, which produces local enhancement in the near field and generates enhanced fluorescence signals in the far field in the emission process. Different tip positions give rise to different enhancement factors, which leads to the tip-position-dependent photon yield. Different modes have different charge distributions owing to different transition dipoles. For a given tip position, the local enhancement produced by the tip will be different for different modes. Overall, the tip position is important for enhancing the optical contrast of photon images through site- and mode-selective enhancement by image charges.

The model used in the simulation of photon images is similar to the one proposed in ref. 14. Here we simplify the STM tip–substrate structure as a combined sphere–plane system. Considering the sphere and the plane as perfect conductors, the images Q' of a certain charge Q for these two surfaces are

$$Q' = -Q \quad \text{and} \quad Q' = -\frac{R_0}{r}Q$$

for the plane and sphere, respectively; the position vectors of the image charges for the first reflection are

$$\mathbf{r}_1^p = (x, y, -z) \quad \text{and} \quad \mathbf{r}_1^s = \frac{R_0^2}{r^2}\mathbf{r}$$

for the plane ('p' superscript) and sphere ('s' superscript), respectively, in which R_0 is the radius of the sphere and \mathbf{r} is the position vector from the centre of the sphere to the charge, as illustrated in Extended Data Fig. 7c, d.

The reflections between two surfaces will result in a series of image charges, and the total dipole moment \mathbf{p}_{tot} of a charge Q positioned in the gap is

$$\begin{aligned} \mathbf{p}_{\text{tot}}(Q) = & Q\mathbf{r}_0 + \left[(-1)Q\mathbf{r}_1^p + (-1)\frac{R_0}{r_1^s}Q\mathbf{r}_1^s\right] + \left[(-1)^2\frac{R_0}{r_1^s}Q\mathbf{r}_2^p + (-1)^2\frac{R_0}{r_2^s}Q\mathbf{r}_2^s\right] + \dots \\ = & Q\left\{\mathbf{r}_0 + \left[(-1)\mathbf{r}_1^p + (-1)\frac{R_0}{r_1^s}\mathbf{r}_1^s\right] \right. \\ & + \sum_{n=1}^{N_r/2} \left[(-1)^{2n}\mathbf{r}_{2n}^p \prod_{m=1}^n \left(\frac{R_0}{r_{2m-1}^s}\right) + (-1)^{2n}\mathbf{r}_{2n}^s \prod_{m=1}^n \left(\frac{R_0}{r_{2m}^p}\right)\right] \\ & \left. + \sum_{n=1}^{N_r/2-1} \left[(-1)^{2n+1}\mathbf{r}_{2n+1}^p \prod_{m=1}^n \left(\frac{R_0}{r_{2m}^s}\right) + (-1)^{2n+1}\mathbf{r}_{2n+1}^s \prod_{m=0}^n \left(\frac{R_0}{r_{2m+1}^p}\right)\right]\right\} \end{aligned}$$

in which N_r is the total number of reflections and is chosen to be an even number because of the presence of two surfaces (substrate plane and tip surface). In our calculation, we use $N_r = 300$ to ensure convergence.

By summing up all the total dipole moments of the charges corresponding to the transition dipoles in the molecular architectures, we obtain the total dipole moment of the whole system: $\mathbf{p}_{\text{tot}} = \sum_i \mathbf{p}_{\text{tot}}(Q_i)$.

The differential radiation power in the far field per solid angle $\frac{dP_{\text{rad}}}{d\Omega}$ is calculated⁴⁵ using

$$\frac{dP_{\text{rad}}}{d\Omega} = \frac{\omega^4}{32\pi^2\epsilon_0 c^3} |\mathbf{p}_{\text{tot}}|^2 \sin^2(\theta)$$

in which θ is the optical detection angle ($\theta = 60^\circ$ with respect to the STM tip axis in our system), ω is the radiation frequency of the dipole and c is the speed of light. By changing the positions of the tip (sphere), we can obtain the real-space distribution of radiation intensity for different distributions of point charges, corresponding to different dipole–dipole configurations. The parameters for simulation are as follows: the radius of the sphere is 1 nm; the distance between the molecular plane and the end of the sphere is 0.8 nm; and the distance between the molecular plane and the substrate is 0.5 nm, according to the thickness of three-monolayer NaCl. The frame size of simulated patterns for a dimer is 6.25 nm \times 5 nm.

Reasonable agreement was achieved between the simulated patterns and experimental images for dimer and oligomer systems, in terms of the numbers and positions of emission maxima and nodes, especially for the two strongest emission modes (modes 1 and 2). This consistency suggests that the simple dipole model used here could provide valuable information on the coherent excitonic coupling features in coupled molecular systems.

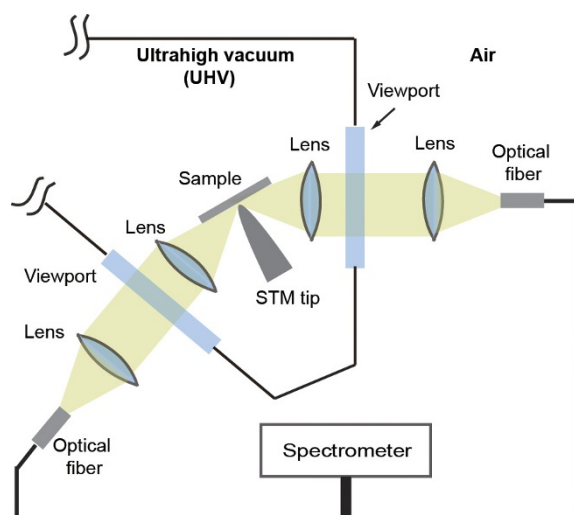
By contrast, the agreement for the photon imaging patterns of modes 3 and 4 is relatively poor. To reproduce the details of the photon imaging patterns for all coupling modes, and precisely calculate the energy differences, more sophisticated theoretical calculations are needed to thoroughly understand the excitation process, the excited states of the coupled molecule systems on dielectric surfaces, and the radiative transitions that originated from delocalized excitons.

Measured exciton coupling strength and oscillation frequency. According to equation (2) and Fig. 3c, d, the coupling strength $|J|$ and energy shifts ΔW presented in Extended Data Table 1 can be determined from the peak positions of different emission modes. The oscillation frequency Ω in the entangled dimer system is calculated via $\Omega = 2|J|/\hbar$ (ref. 27). The coupling strengths for in-line and parallel coupling types are obtained from the following peak values for different emission modes of a ZnPc dimer: 1,887.4 \pm 0.3 meV (mode 1), 1,896.0 \pm 0.3 meV (mode 2), 1,898.9 \pm 0.3 meV (mode 3), 1,912.4 \pm 0.3 meV (mode 4), and 1,921.9 \pm 0.3 meV (mode 5). The peak energy for a ZnPc monomer is 1,899.2 \pm 0.6 meV. These peak energy values for the dimer are obtained from statistical analyses over eight data sets acquired with the same tip under the same NCP resonance condition. The STML spectra used for these analyses were acquired over the strongest emission site for each mode with a spectral resolution of about 0.2 nm (0.7 meV; calibrated by the 546 nm Hg line) using a grating of 1,200 grooves per mm and a slit width of 25 μm .

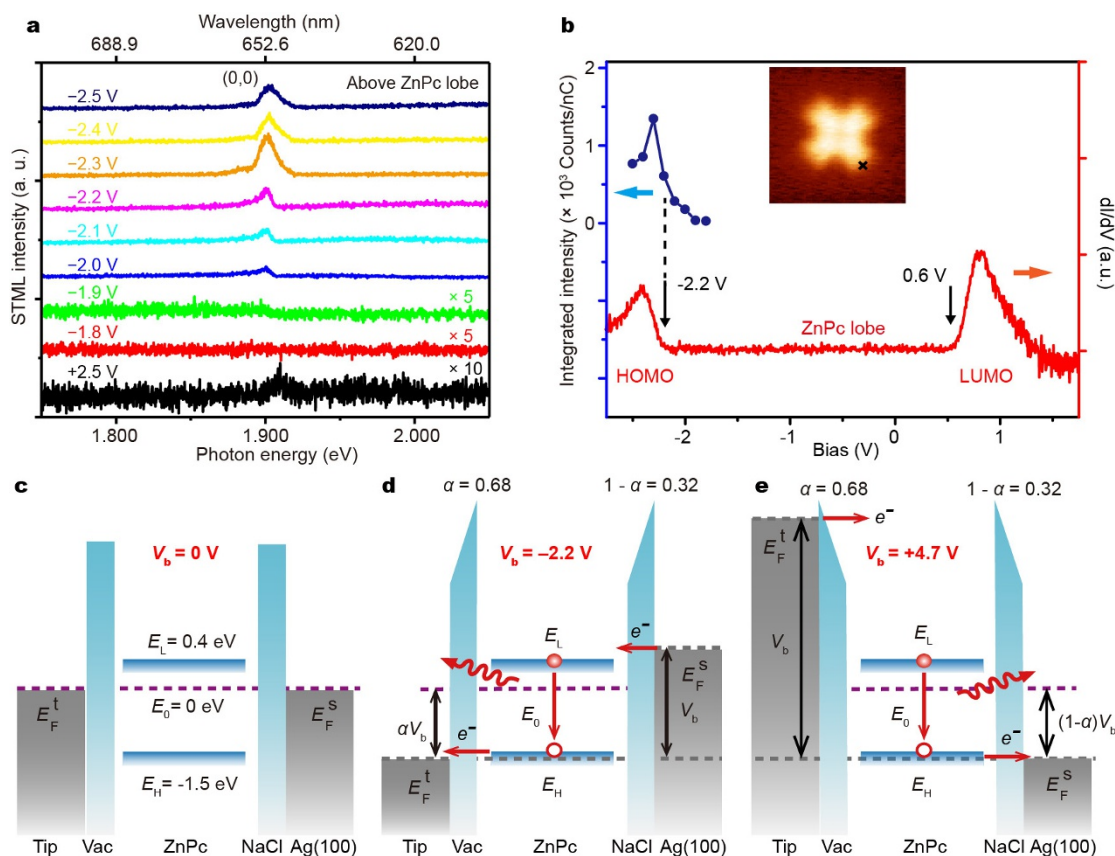
The experimentally determined coupling strength $|J|$ for the in-line dipole coupling (approximately 17.3 meV) was found to be nearly twice of that for the parallel coupling (approximately 8.2 meV), as predicted by the theoretical model given in equation (4). This consistency, together with the reasonable agreement between the experimental photon imaging patterns and the simulated ones, suggests that the dipole–dipole coupling captures the essence of the excitonic coupling in coupled molecular systems.

- Hoffmann, G., Libioulle, L. & Berndt, R. Tunneling-induced luminescence from adsorbed organic molecules with submolecular lateral resolution. *Phys. Rev. B* **65**, 212107 (2002).
- Zhang, C., Chen, L. G., Zhang, R. & Dong, Z. C. Scanning tunneling microscope based nanoscale optical imaging of molecules on surfaces. *Jpn. J. Appl. Phys.* **54**, 08LA01 (2015).
- Crommie, M. F., Lutz, C. P. & Eigler, D. M. Confinement of electrons to quantum corrals on a metal surface. *Science* **262**, 218–220 (1993).
- Manoharan, H. C., Lutz, C. P. & Eigler, D. M. Quantum mirages formed by coherent projection of electronic structure. *Nature* **403**, 512–515 (2000).
- Zhao, A. D. *et al.* Controlling the Kondo effect of an adsorbed magnetic ion through its chemical bonding. *Science* **309**, 1542–1544 (2005).
- Wu, S. W., Nazin, G. V., Chen, X., Qiu, X. H. & Ho, W. Control of relative tunneling rates in single molecule bipolar electron transport. *Phys. Rev. Lett.* **93**, 236802 (2004).
- Meng, Q. *et al.* Tunneling electron induced molecular electroluminescence from individual porphyrin J-aggregates. *Appl. Phys. Lett.* **107**, 043103 (2015).
- Le Moal, E., Müller, M., Bauer, O. & Sokolowski, M. Misfit driven azimuthal orientation of NaCl domains on Ag(100). *Surf. Sci.* **603**, 2434–2444 (2009).
- Gouterman, M. In *The Porphyrins* Vol. III (ed. Dolphin, D.) Ch. 1, 1–165 (Academic Press, 1978).

40. Minaev, B., Wang, Y.-H., Wang, C.-K., Luo, Y. & Ågren, H. Density functional theory study of vibronic structure of the first absorption Q_x band in free-base porphyrin. *Spectrochim. Acta A* **65**, 308–323 (2006).
41. Lu, X., Grobis, M., Khoo, K. H., Louie, S. G. & Crommie, M. F. Spatially mapping the spectral density of a single C_{60} molecule. *Phys. Rev. Lett.* **90**, 096802 (2003).
42. Beenken, W. J. D. & Pullerits, T. Excitonic coupling in polythiophenes: comparison of different calculation methods. *J. Chem. Phys.* **120**, 2490–2495 (2004).
43. Sun, M., Chen, J. & Xu, H. Visualizations of transition dipoles, charge transfer, and electron-hole coherence on electronic state transitions between excited states for two-photon absorption. *J. Chem. Phys.* **128**, 064106 (2008).
44. Zhou, X., Ren, A.-M., Feng, J.-K. & Liu, X.-J. Theoretical studies on the one- and two-photon absorption of tetrabenzoporphyrins and phthalocyanines. *Can. J. Chem.* **82**, 19–26 (2004).
45. Le Ru, E. & Etchegoin, P. *Principles of Surface-Enhanced Raman Spectroscopy and Related Plasmonic Effects* Ch. 2 (Elsevier, 2008).

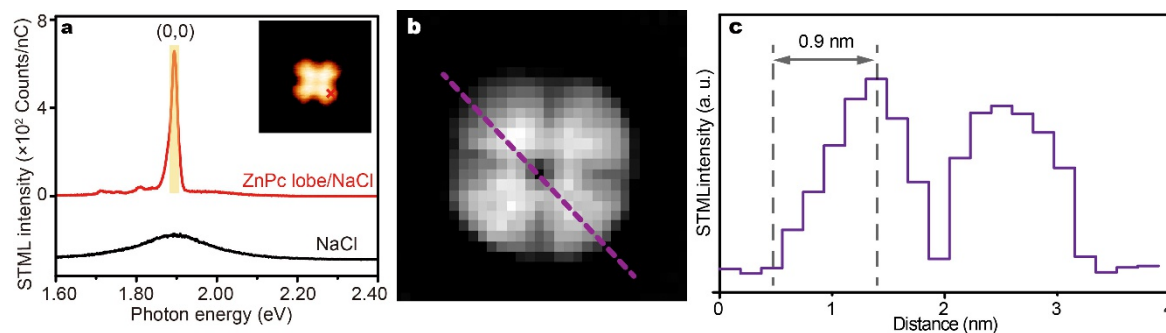


Extended Data Figure 1 | Schematic of our experimental set-up for a combined system of low-temperature ultrahigh-vacuum STM with optical detections. The highly localized tunnelling electrons in a STM are used to excite light emission from the STM junction through inelastic tunnelling. This technique is called STM-induced luminescence (STML). In our system, photons emitted from the STM junction were collected by a two-channel double-lens system to increase the collection efficiency. The total hemisphere photon collection efficiency for the two-channel double-lens system is about 20%. The spectra were measured with a liquid-nitrogen-cooled charge-coupled device spectrometer (Princeton Instruments). Different gratings (150 grooves per mm, 600 grooves per mm and 1200 grooves per mm) and slits (100 μm and 25 μm) were used in spectral measurements for different requirements on wavelength ranges and spectral resolutions. All spectra presented in this paper are not corrected for the wavelength-dependent sensitivity of photon detection systems.



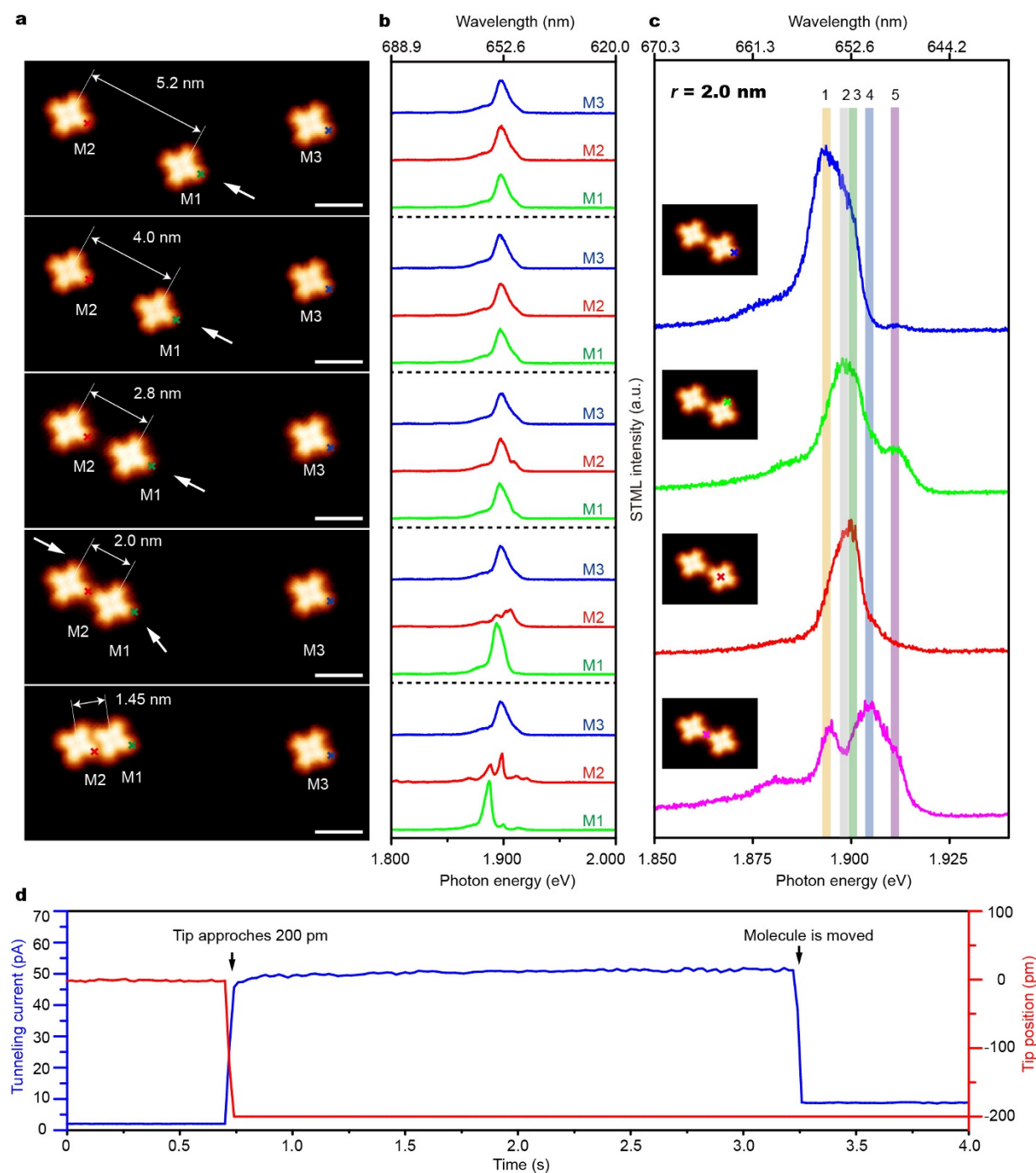
Extended Data Figure 2 | Excitation mechanism in STML. **a**, STML spectra acquired above the lobe of a single ZnPc molecule on the NaCl island at different excitation biases, as indicated (10 pA, 60 s). **b**, dI/dV spectra acquired at the ZnPc lobe (red line) using the lock-in technique. The tunnelling gap was set at -2.5 V and 50 pA. The bias modulation was 20 mV (r.m.s.) at 329 Hz. The molecular emission intensities over a different excitation bias is also plotted as a blue line and filled circles

(integrated spectral range: 1.86–1.94 eV). The inset shows an STM image of a ZnPc molecule ($3 \text{ nm} \times 3 \text{ nm}$; -1.7 V, 2 pA) with the 'x' marking the position for both the dI/dV and STML measurements in **a**. **c–e**, Sketch of a double-barrier junction showing the energy-level alignments of the HOMO and LUMO at different bias voltages: $V_b = 0$ V (**c**), $V_b = -2.2$ V (**d**) and $V_b = +4.7$ V (**e**). $E_F^{t/s}$, Fermi energy of the tip/substrate.



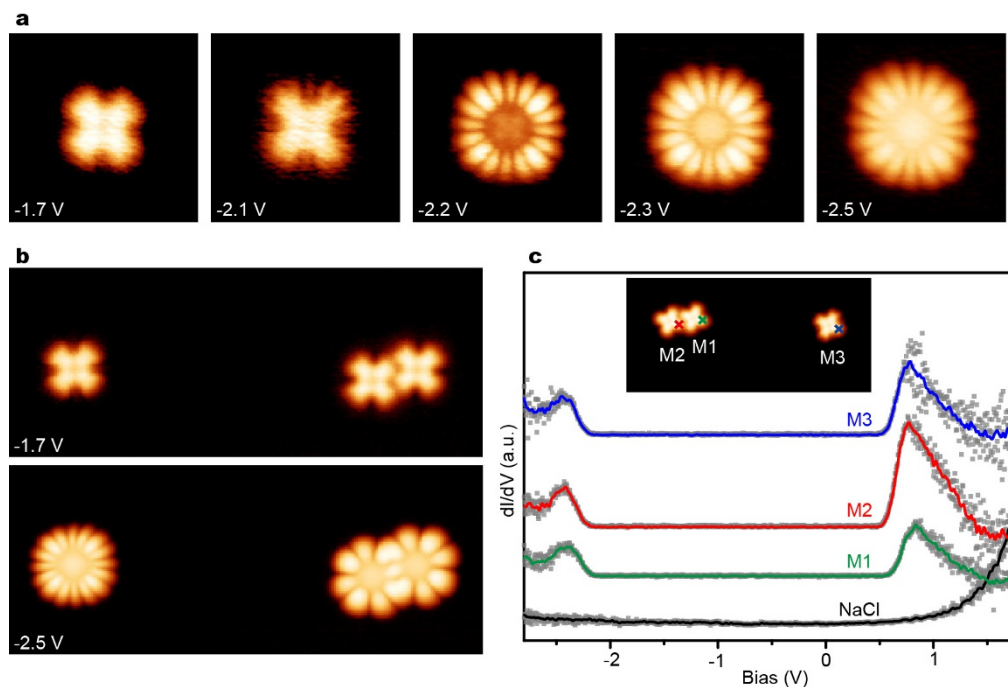
Extended Data Figure 3 | Sub-nanometre spatial resolution of spectroscopic imaging. **a**, STML spectrum (-2.5 V, 200 pA, 60 s) acquired at the lobe of an isolated ZnPc monomer on NaCl (top curve, red), indicated by the 'x' in the inset (-1.7 V, 2 pA; 4 nm \times 4 nm). The NCP emission spectrum (bottom curve, black) acquired on the NaCl surface is shown as a reference. **b**, Energy-resolved photon imaging pattern of a single ZnPc molecule on NaCl by integrating the molecule-specific

fluorescence signals over the energy range 1.89 – 1.91 eV, indicated by the yellow shading in **a** (4 nm \times 4 nm, 30×28 pixels; -2.5 V, 200 pA, 5 s per pixel). **c**, STML intensity profile for the (purple dashed) line trace in **b**. The line-profile analysis has a spatial resolution of less than 1 nm (about 0.7 nm estimated within a 10% – 90% contrast), showing the change of contrast from 0% to 100% over a distance as short as 0.9 nm.



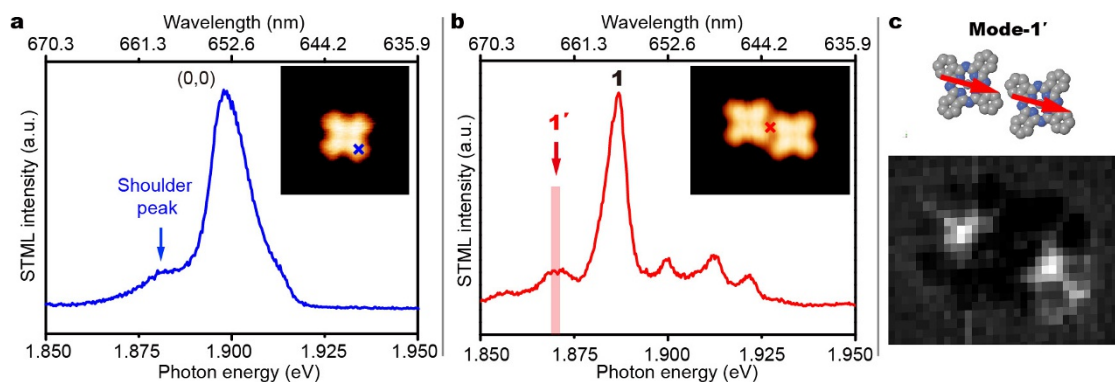
Extended Data Figure 4 | Spectral evolution with varied intermolecular distances. **a**, STM images taken during the manipulation process (-1.7 V, 2 pA). There are three isolated ZnPc molecules adsorbed on NaCl marked as M1, M2 and M3. M3 is used as a reference molecule. M1 and M2 are pushed together, as indicated by the white arrows for manipulation directions. The intermolecular centre-to-centre distance r between M1 and M2 is marked. Scale bars, 2 nm. **b**, Corresponding electroluminescence spectra (-2.5 V, 200 pA, 60 s) collected from the lobes of the three ZnPc molecules, as indicated by the 'x's in **a**. **c**, Representative site-dependent

STML spectra (-2.5 V, 200 pA, 60 s) for $r = 2.0$ nm acquired at the respective 'x' positions in the insets images (4.6 nm \times 6 nm, -1.7 V, 2 pA). The shaded regions labelled 1–5 mark the possible peak positions induced by the coherent dipole–dipole interaction. **d**, Typical current–time and tip–position–time curves during the manipulation process. First, we placed the STM tip close to the edge of the lobe of a ZnPc molecule on NaCl. Second, we turned off the feedback and approached the tip to the molecule by about 200 pm (set point: $+2.5$ V, 2 pA). In this way, the ZnPc molecule was found to move away from the STM tip.



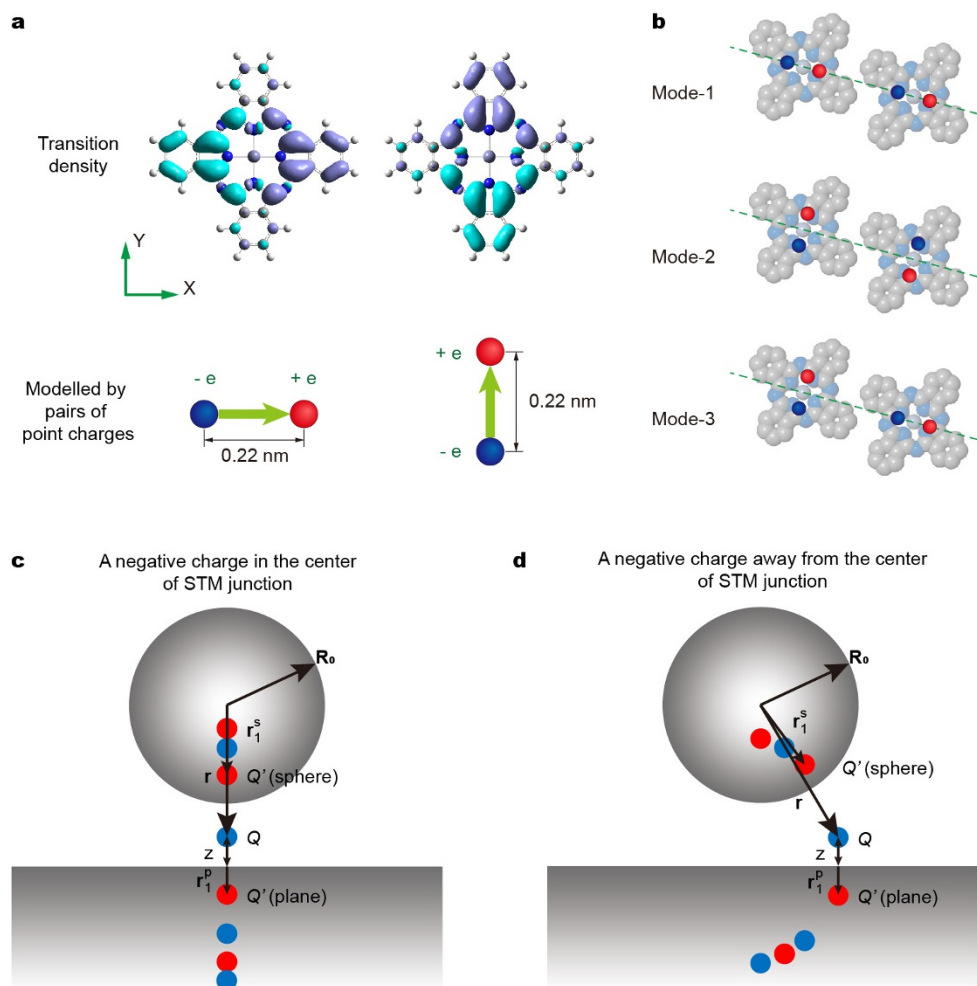
Extended Data Figure 5 | Bias-dependent features of STM images and dI/dV spectra for isolated ZnPc monomers and ZnPc dimers on the NaCl surface. **a**, STM images of an isolated ZnPc monomer acquired at different biases (4 nm \times 4 nm; 2 pA). The cross-like feature is observed when the bias is set inside the HOMO–LUMO gap (for example, -1.7 V), revealing the characteristics of the molecular skeleton. The rotating behaviour of an isolated ZnPc monomer is evident at about -2.2 V, giving rise to a 16-lobe-like pattern instead of the 8-lobe-like pattern associated with the HOMO state for a immobilized ZnPc. **b**, STM images of an isolated ZnPc monomer and a ZnPc dimer at different biases (15 nm \times 6 nm; 2 pA). The rotation of ZnPc is blocked when in contact with another ZnPc owing to the steric hindrance, as indicated by the appearance of an 8-lobe-like

pattern of the component ZnPc monomer in the dimer. **c**, dI/dV spectra were acquired at the ZnPc lobes of M1, M2 and M3, as indicated in the inset (15 nm \times 7 nm, -1.7 V, 2 pA). The dI/dV spectrum on the bare NaCl surface is also shown as a reference. The smoothed dI/dV curves are presented in colour; the raw data are represented as grey squares. The dI/dV signals were measured using the lock-in technique. The tunnelling gap was set at -2.5 V and 20 pA. The bias modulation was 20 mV (r.m.s.) at 329 Hz. The dI/dV spectra are offset for clarity. No noticeable difference in peak positions was observed between the dI/dV curves acquired from both the isolated ZnPc monomer and the ZnPc dimer. However, the STML spectral features from the dimer are markedly different to those of an isolated ZnPc monomer (Fig. 2).



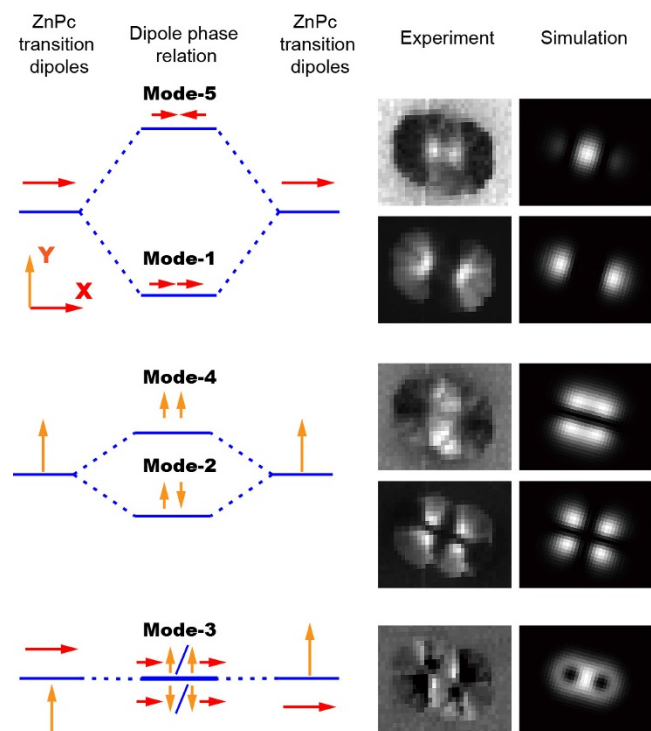
Extended Data Figure 6 | Origin of the emission peak at about 1.870 eV from the ZnPc dimer. **a**, STML spectrum (-2.5 V, 200 pA, 60 s) acquired at a lobe of the isolated ZnPc molecule, as indicated in the inset (4 nm \times 4 nm; -1.7 V, 2 pA), showing the Q-band emission containing a shoulder peak at 1.882 eV (about 659 nm). **b**, STML spectrum (-2.5 V, 200 pA, 60 s) acquired at the centre of the ZnPc dimer, as indicated in the

inset (5 nm \times 4 nm; -1.7 V, 2 pA), showing an additional peak at 1.870 eV (about 663 nm) labelled as mode $1'$. **c**, Photon imaging pattern acquired by integrating the spectral range corresponding to the mode- $1'$ emission (-2.5 V, 200 pA, 5 s per pixel; frame size: 5 nm \times 4 nm, 34×21 pixels; integration range: $1,870 \pm 1.5$ meV, shaded region in **b**).

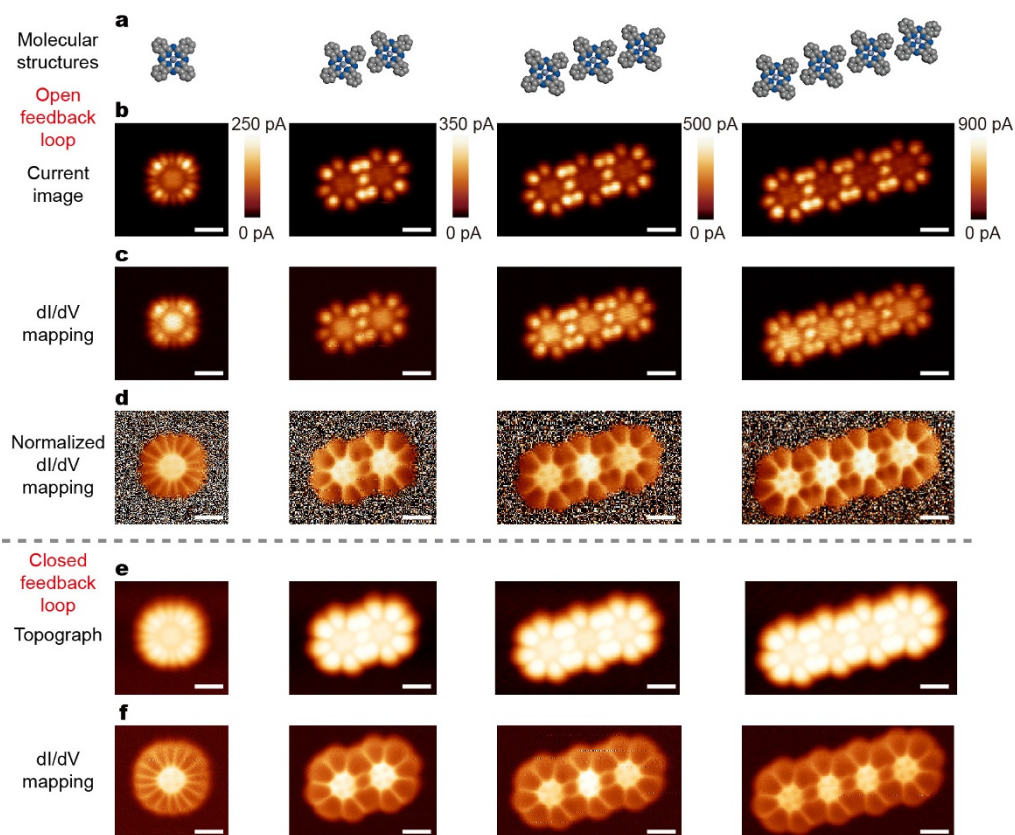


Extended Data Figure 7 | Theoretical simulation of real-space STML mapping. a, Modelling the transition dipoles of the ZnPc monomer by pairs of opposite point charges. The top images show the distribution of two equivalent transition densities associated with the corresponding transition dipoles of a ZnPc molecule. Positive and negative transition densities are represented by the violet and cyan shading, respectively, which are superimposed on the ball-and-stick model of a ZnPc molecule (the H, C, N

and Zn atoms are represented by the white, grey, blue and violet spheres, respectively). **b,** Arrangements of the orientations for the pair of point charges for selected examples of coupling modes (modes 1, 2 and 3) in our simulations. The distance between the two opposite charges in the schematic is exaggerated for clarity. The green dashed lines mark the centre-to-centre axial direction of the dimer. **c, d,** Schematic of the image-charge models when the tip is centred over the molecule (**c**) or off-centre (**d**).

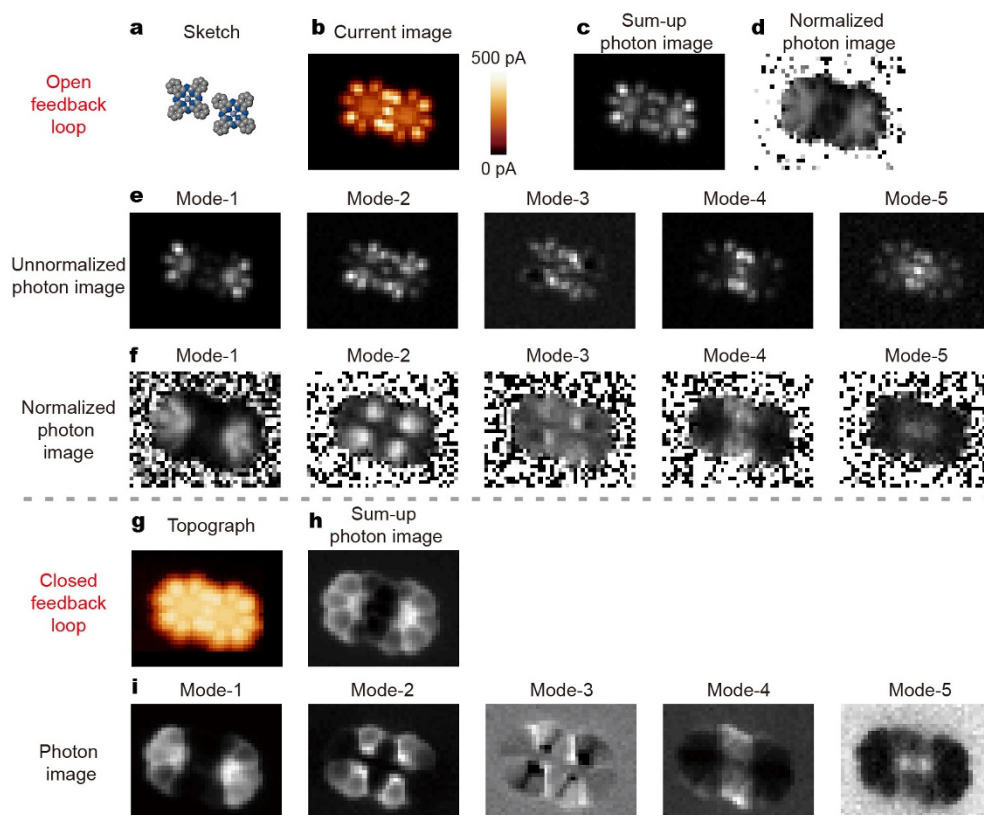


Extended Data Figure 8 | Analogy to the bonding/anti-bonding-like features of σ and π orbitals. To better view the analogy, the experimental and simulated patterns in Fig. 3 are reorganized as 'bonding-like' and 'anti-bonding-like' pattern pairs. The left column shows the schematic diagrams of different modes corresponding to different coherent dipole-dipole coupling arrangements in terms of transition-dipole orientations and related phase relations. The corresponding experimental and simulated patterns are plotted in the middle and right columns.



Extended Data Figure 9 | dI/dV mapping data for a ZnPc monomer, dimer, trimer and tetramer acquired with an open or closed feedback loop. **a**, Sketch of ZnPc molecular configurations. **b**, **c**, Current images (**b**) and dI/dV images (**c**) for different ZnPc molecular configurations acquired simultaneously with an open feedback loop (-2.5 V). The bias modulation was 10 mV (r.m.s.) at 329 Hz. **d**, Corresponding normalized dI/dV images obtained by dividing the tunnelling current pixel by pixel.

e, **f**, STM images (**e**) and dI/dV images (**f**) for different ZnPc molecular configurations acquired simultaneously with a closed feedback loop (-2.5 V, 100 pA). The bias modulation was 10 mV (r.m.s.) at 329 Hz. For the measurements of dI/dV mapping and spectroscopic imaging with an open feedback loop, we positioned the tip above the NaCl surface (-2.5 V, 2 pA), switched off the feedback loop, lifted the tip up by 150 pm and started scanning over the selected area with molecules. Scale bars, 1 nm.



Extended Data Figure 10 | Spectroscopic imaging of a ZnPc dimer with an open or closed feedback loop. **a**, Sketch of a ZnPc dimer. **b**, **c**, Current image (**b**) and sum-up photon image (integrated over 1.86–1.94 eV) (**c**) acquired simultaneously with an open feedback loop (5.2 nm × 4 nm, 39 × 30 pixels; −2.5 V, 1 s per pixel). **d**, Corresponding normalized sum-up photon image obtained by dividing the sum-up image by the tunnelling

current image pixel by pixel. **e**, Un-normalized photon images for each mode. **f**, Corresponding normalized photon images for each mode in (**e**). **g**, **h**, For comparison, a spectroscopic image on the same ZnPc dimer is acquired with a closed feedback loop. STM image (**g**) and sum-up photon image (integrated over 1.86–1.94 eV) (**h**) (5.2 nm × 4 nm, 39 × 30 pixels; −2.5 V, 200 pA, 2 s per pixel). **i**, Photon images for each mode.

Extended Data Table 1 | Experimentally determined exciton coupling strength $|J|$ and oscillation frequency Ω

	$ J $ (meV)	ΔW (meV)	Ω (s ⁻¹)
$\rightarrow \rightarrow / \rightarrow \leftarrow$	17.3 ± 0.3	5.5 ± 0.9	$\sim 5.3 \times 10^{13}$
$\uparrow \downarrow / \uparrow \uparrow$	8.2 ± 0.3	5.0 ± 0.9	$\sim 2.5 \times 10^{13}$

Also listed are the energy differences of van der Waals interaction between the excited and ground states of the dimer (ΔW). The arrow pattern $\rightarrow \rightarrow / \rightarrow \leftarrow$ in the first column indicates exciton splitting between the in-line in-phase and in-line out-of-phase coupling modes; the arrow pattern $\uparrow \downarrow / \uparrow \uparrow$ indicates exciton splitting between the parallel out-of-phase and parallel in-phase coupling modes.